Modelling, simulation and optimization for a SThm nanoprobe

Bin Yang*, Michel Lenczner†, Scott Cogan*, Bernd Gotsmann‡ Pawel Janus§ and Guillaume Boetch¶
*FEMTO-ST, University of Franche-Comté, Belfort, France, bin.yang@femto-st.fr
†FEMTO-ST, University of Technology at Belfort-Montbeliard, France, michel.lenczner@utbm.fr
‡IBM Research-Zürich, Säumerstrasse 4, Ch8803 Rüschlikon, Switzerland, bgo@zurich.ibm.com
§ Institute of Electron Technology al. Lotnikow 32/46 02-669 Warszawa, PL, janus@ite.waw.pl
¶Imina Technologie SA, EPFL Innovation Park Batiment E, 1015 Lausanne, Switzerland, guillaume.boetsch@imina.ch

Abstract

This paper presents modelling, simulation and optimization results for a novel SThm probe. The model takes into account thermo-electro-mechanical equations. Moreover, a tip-surface contact model derived by taking into account microscopic multi-asperity contact is proposed and discussed. Results of multi-objective optimization are reported, and finally a multi-scale model that should reduce the simulation time is stated.

KEY WORDS: *Scanning thermal microscopy, Nanoprobe, Tip-surface contact, Interface thermal conductance, Multi-objective optimization, Asymptotic model*

1. Introduction

Modern technology of micro/nanoelectronic components, sensors and MEMS/NEMS (Micro/Nano-Electro-Mechanical-Systems) requires increasingly the control of materials at the sub-micrometer down to the nanometer scale. Additionally, the heat transfer phenomena, including e.g. phonon heat conduction mechanism in micro- and nanostructures, may differ significantly from that on the macroscale. Therefore, micro- and nanometer resolution is required for most of the experiments.

Scanning Thermal Microscopy (SThM) is a versatile scanning probe technique allowing for high resolution mapping of the thermal properties and temperature of various substrates. SThM, as every AFM (Atomic Force Microscopy) related technique enables study at micro- and nanoscale which allows designers to better the understanding of heat transport in micro- and nanoelectronic devices.

The invention of the scanning tunneling microscope (STM) [2] and the atomic force microscope (AFM) [1] have allowed sub-micrometer and, at times, atomic scale spatially resolved imaging of surfaces. The spatial resolution of these near-field techniques is only limited by the active area of the sensor (which in the case of STM may only be a few atoms at the end of a metal wire). As described by Dinwiddie and Pylkki in 1994, first scanning thermal microscopy (SThM) probes employed resistance thermometry to measure thermal properties [3]. These probes were fashioned and made from Wollaston process wire consisting of a thin platinum core (ca. 5 μm in diameter) surrounded by a thick silver sheath (ca. 75 μm). Because of its high endurance, Wollaston probe is attractive for microsystem diagnostics [16], however the active area in the range of a few micrometers does not allow quantitative thermal investigations at the nano-scale.

In this paper, we present and discuss a new thermal probe that is designed to achieve quantitative measurement in the range of few tenths nanometers. Two aspects of its modelling are discussed. Since the current models and theories are not sufficient to describe and predict the heat flow through the tip-sample interface and in the vicinity of the contact, a simple model of tip-sample heat transfer is stated. It is obtained by combining recent published results and experimental observations. In addition, a thin plate model is described that includes the three involved physical phenomena as well as the multilayered structure of the probe. It should be useful to reduce the simulation time and so to facilitate optimization. The latter has been carried out using an in-house developed software package SIMBAD for robust optimization and its connection with the FEM simulation software package COMSOL. Three objective optimization results are reported, namely to decrease the thermo-mechanical tip deflection, to increase the Joule heating effect in the tip and to increase the sensitivity of the piezoresistive sensor.

The paper is organized as follows. Section 2 present the probe design. In Section 3, the mathematical formulation of the physical problem is stated. Section 4 is dedicated to the tip-sample heat transfer model. Section 5 presents the SIMBAD-COMSOL package. In Section 6, a parametrization of the SThm probe is introduced allowing to perform the sensitivity analysis and then multi-objective optimizations. The thin plate model is presented in the last section.

2. The probe design

The novel type of nanosensor, described in this paper, is equipped with sharp, conductive tip, an integrated deflection sensor, and an actuation system. A modification of a double sided silicon micromachining process developed for manufacturing of piezoresistive AFM microprobes has been adapted to fabricate SThM sensors [7][8].

Proposed nanoprobes, as the only SThM/ECM probes on the market are integrated with deflection detection, which will significantly improve the system versatility and will enable new applications. As the NANOHEAT system

as free of the bulk and complicated optical deflection sensors, it can be used in small SEM chambers. The

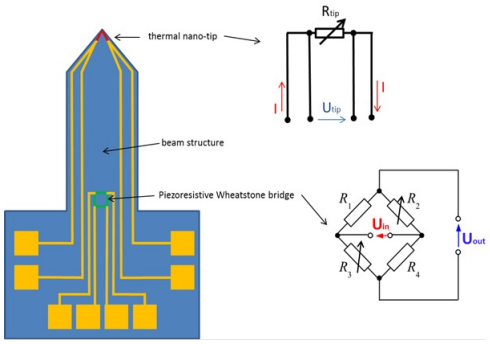

(a) Schematic view of NANOHEAT SThm probe

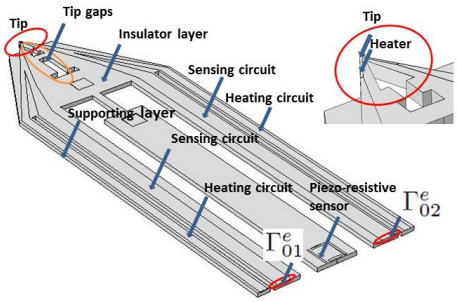

(b) First design of the cantilever

Figure 1. NANOHEAT SThM probe

described SThM nanoprobes are designed to operate in two modes: a) as a passive thermosensing element or b) as an active heat flux meter. In the latter case, a larger current is passed through the resistive tip probe. The power that is required to maintain a constant temperature gradient between the tip and the sample corresponds to the local thermal conductivity of the sample. During active measurements temperature of the tip is increased by $20-30$ K above room temperature. In order to perform quantitative measurements of heat transport between the tip and the surface several crucial criteria have to be met:

-low thermal mass of the microtip allowing for AC thermal measurements (e.g. in the range of 10 kHz)

-high mechanical stiffness of the microtip. This ensures high endurance of the thermal sensor, which is brought into contact while surface scanning.

-low stiffness of the SThM cantilever, which is brought in contact with the investigated surface. The low stiffness of the SThM cantilever will enable surface measurements with relatively low load forces. As a consequence the tip wear is reduced and the sample is not modified.

-high thermal resistance of the SThM cantilever and tip's support. The high thermal resistance of the cantilever will reduce the heat transfer from the thermal tip to the cantilever supporting body. The effective thermal mass of the SThM sensor will be reduced, and its influence on the thermal behavior of the investigated structure will be minimized.

Moreover, the heat transferred from the tip to the cantilever base causes parasitic deflection of the sensor and may influence signal from Wheatstone bridge. First results of modeling and simulations exhibit significant parasitic, 200 nm deflection of the cantilever due to tip's heating by 11 degrees above the room temperature.

According to the applications, developed SThM nanoprobe will enable surface measurements in contact scanning probe microscopy mode at load force ranging from 10 nN up to 1 microN. The load force will be detected with the resolution of 10 pN in the bandwidth of 100 Hz. The low load forces as well as sub-nanometer vertical spatial resolution in the range will be needed in investigations of graphene and molecular samples, whereas the high force will be applied in investigations of high-k insulators.

3. Mathematical model description

The SThm probe is designed as a three-layered structure. The silicon supporting layer has a thickness of 5 μm, it is covered by a 50 nm *SiO2* layer where 100 nm thick platinum tracks are deposited. The latter consists of a heating circuit, a sensing circuit and a sharp resistive tip. The three corresponding domains are denoted by Ω_{Si}, Ω_{SiO2} and Ω_{Pt} and Ω denotes their union.

In Figure 1(b), the two inner platinum legs constitute the heating circuit and the two outer constitute the sensing circuit. A piezo-resistive sensor for stress measurement is located to the base of the probe, it is used to measure the tip displacement.

In all the paper, the Einstein summation convention is adopted. We use $\mathbf{C}^q$, $\mathbf{M}^q$, $\mathbf{k}^q$ where $q \in \{\mathrm{Pt}, \mathrm{SiO2}, \mathrm{Si}\}$ and $\mathbf{a}$, to denote the tensor of elasticity, the matrix of thermal expansion, the matrix of thermal conductivity in each layer and the matrix of electric conductivity in platinium. We denote by $\mathbf{u}$, T, and φ the vector of mechanical displacements, the difference of the temperature to the ambiant temperature and the electric potential. The system is governed by the following equations,

$$\begin{cases} -\operatorname{div}(\sigma) = \mathbf{f} \text{ in } \Omega \\ -\operatorname{div}\mathbf{q} = (\nabla\varphi)^T \mathbf{a} \nabla\varphi \text{ in } \Omega_{\mathrm{Pt}} \\ -\operatorname{div}\mathbf{q} = 0 \text{ in } \Omega \backslash \Omega_{\mathrm{Pt}} \\ -\operatorname{div}(\mathbf{a}\nabla\varphi) = 0 \text{ in } \Omega_{\mathrm{Pt}} \end{cases} \tag{1}$$

where $\mathbf{a} = (1+\alpha T)^{-1}\mathbf{a}^{ref}$, $\mathbf{f}$ is the body force load, $\sigma = \mathbf{C}^q \mathbf{s}(\mathbf{u}) + \mathbf{M}^q(T)$ is the tensor of mechanical stresses, $\mathbf{s}(\mathbf{u}) = \frac{1}{2}(\nabla u + \nabla u^T)$ is the tensor of strains, $\mathbf{q} = \mathbf{k}^q \nabla T$ is the heat flux, $\mathbf{a}^{ref}$ is the tensor of electric conductivity at ambiant temperature, and α is the thermal coefficient.

Regarding the boundary conditions, the cantilever is clamped and with an imposed temperature on a part Γ_0 of the boundary, i.e. $\mathbf{u} = 0$ and $T = T_0$, and it is left free of load and thermally insulated on the other part, i.e. $\sigma\mathbf{n} = 0$ and $\nabla T.\mathbf{n} = 0$ where $\mathbf{n}$ denotes the outward unit normal vector to the boundary. Finally, a current source

is applied to Γ^e_{01} and Γ^e_{02} is grounded, see Figure 1(b). The tip-sample interface condition is discussed in details in the next section, however it has not yet been taken into account in the other parts of the paper which are focused on the probe itself but not yet on its interaction with a sample.

4. Heat transfer through the tip surface contact

Scanning thermal microscopy probes the heat transfer between the integrated heater/sensor of a scanning probe cantilever and a sample surface. The heat flux across the tip-surface contact directly relates to the measured quantities, namely the thermal resistance into or out of the sample, which is to be related to thermal conductivity of the sample, and the sample temperature [14]. For a quantitative understanding and simulation of the tip-sample heat transfer, it is essential to quantify this thermal resistance and its dependence on the interface parameters. A schematic of the tip-surface contact and

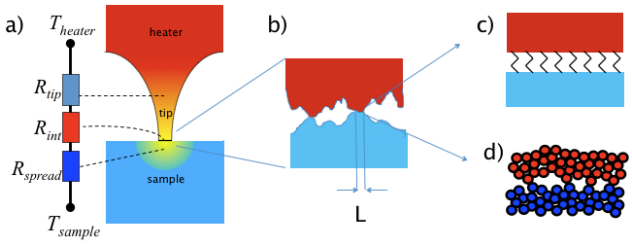

Figure 2. a) Schematic of the tip-sample heat transfer b) a microscopic multi-asperity contact c) an atomic scale interface d) atomic-scale roughness.

the associated thermal resistances are shown in Fig. 2 a). Scanning thermal microscopy tips are typically designed such that the thermal resistance of the tip R_{tip} is small compared the contribution of the sample R_{sample}. This is achieved by choosing good thermal conductors such as metals or silicon as tip materials. However, in quest of achieving high spacial resolution, the dimensions of the tip become smaller and as a consequence its thermal resistance becomes significant. In the case of silicon tips the phonon mean free path of about 100 nm at room temperature exceeds the diameter of the tip.

As a consequence, diffusive thermal transport as simulated in finite element modeling cannot be directly applied any longer. Instead, heat conduction through the tip is modeled as quasi-ballistic transport. For example, following the expression of thermal conductivity from kinetic theory: $k = Cv\Lambda$, with k being the thermal conductivity, C the heat capacity per unit volume, v the phonon velocity, and Λ the mean free path, one can apply Mathiessen's rule to calculate a mean free path modified from the bulk value through boundary scattering. For simple geometries such as conical, analytic expressions exist [5].

The thermal resistance of the sample can be calculated in a similar manner. If the characteristic length scale of the spreading resistance into the sample, the contact diameter, is much larger than the average mean free path of heat carriers in the sample, then diffusive transport leads to a scaling with the inverse of the contact diameter. In contrast, the resistance within the sample scales inversely proportional to the contact area in the ballistic transport regime. For spherical contact areas, both cases can be described with a single analytic interpolation formula.

The contributions from tip and sample to the resistance can be calculated with existing and established models, for simple geometries even using analytic equations. The contribution of the interface, however, is more complicated because both phonon mismatch and mechanical contact geometry have to be taken into account. Phonon mismatch, i.e. the difference in phonon dispersion between two solids, causes a thermal interface resistance (or thermal boundary resistance). Even for interfaces of perfect quality this leads to an appreciable resistance [15]. In reality, however, the interface quality is not perfect, due to oxide layers, non-continuous contact areas, or weak coupling bonds between the atoms of either solid. To account for the weak coupling, advanced contact models have been developed in which the transmission probability is related to the mechanical coupling spring between the two solids [12], [11].

In SThM there are further aspects to be considered. Due to the roughness of the tip and sample surfaces, the apparent contact area may in fact be divided into smaller contact spots. Appropriate modeling of this effect depends on the length scale L of the contact spots. If L is much larger than the mean free path of heat carriers than the solutions mentioned above can be applied. If L is smaller than the mean free path then ballistic solutions play a role. This has been pointed out for example by Prasher and Phelan [13]. As discussed recently [10], [4], the notion of finite contact spots may be extrapolated to the atomic scale. This can lead to a situation in which the contact spot diameter L is smaller even than the coherence length λ_{coh} of the phonons while the distance between individual contact spots may exceed λ_{coh}. In this regime, quantization of conductance may occur [4].

Including all these aspects into the modeling of the tip-surface contact requires taking all relevant length scales into account. Some of the effects mentioned above, namely the weak coupling between tip and sample as well as the effect of roughness on the contact area, are experimentally observed in the form of pressure dependence of the interface resistance. This effect will increase thermal conductance with applied load (together with an increased nominal contact area of a curved tip pressed into a surface). The magnitude of the load-dependence can therefore be an indication of the transport regime.

Following experimental data on the pressure dependence of conductance across weak interfaces [6] gives us

an order of magnitude of the interface conductance

$$g_{int}(p) = g_0 + g_1\, p$$

with g_{int} the interface conductance in units of W/(m^{2}K), g_0 around 4×10^7 W/(m^{2}K), p the pressure at the interface and g_1 on the order of 10^{-2} W/(NK). In contrast, for systems that may involve quantized transport pressure dependencies on the order of 1 W/(NK) have been reported. At sufficiently high pressures the pressure-dependence of the thermal conductance reduces again [6], [4]

5. Simbad a tool for optimization

The software SIMBAD provides a generic simulation-based design tool for investigating the behaviour of complex modeled systems. A MATLAB link has been set between COMSOL and SIMBAD so that COMSOL models may be used as an input for a design under SIMBAD. It includes the definition of the optimization problem: the initial value of parameters, the parameter relative ranges, the objective features and the constraints for geometry and objective features. It serves to transmit current parameters between the two software packages.

Three SIMBAD toolboxes have been used. The design sensitivity and effects analysis toolbox is used to quantify the impact of design variable modifications on the design objective of interest. It allows the design space to be reduced to the subset of influential variables. The multi-objective performance optimization toolbox is used to obtain an approximation of the Pareto front for the different design objectives. It provides the analyst with a useful indicator on the trade-offs between the objectives of interest. Finally, the model validation and uncertainty quantification is used to quantify the impact of both aleatory and epistemic (lack of knowledge) uncertainties in the design variables and system environment on the design objectives and constraints.

6. Optimization

The first step in optimization consists in building a full parametrization of the probe geometry, see Fig 3. The geometric parameters are updated during the sensitivity analysis as well as the optimization loops. According to the applications of this probe, three objectives are set, the maximization of the maximum temperature $T_{\max} = \max_{x\in\Omega} T(x)$, the minimization of the maximum vertical mechanical displacement $u_{\max} = \max_{x\in\Omega} u_3(x)$ for a fixed voltage source and no body force load and the maximization of the mean value σ_{mean} of the sensor stress i.e. the von-Mise stress in the piezoresistive sensor for a prescribed tip displacement. The multi-objective optimization is carried with two different simulation conditions. To optimize $T_{\max}$ and $u_{\max}$, only the voltage source is imposed at 0.12 V. Then, the optimized value of σ_{mean} is found by fixing a 1 μm tip displacement.

In the following discussion, we distinguish between the original design shown in Figure 1(b) whose initial parameters are provided by the probe designers, and the nominal design shown in 3 whose initial parameters come from a preliminary optimization. The parameters of the original design are splitted into three groups of layer thicknesses, leg dimensions and tip gaps. The latter includes the triangle-shaped and T-shaped gaps near the tip.

In the first group, both $T_{\max}$ and $u_{\max}$ are increasing with the platinum layer thickness and decreasing with the silicon layer thickness, and the sensor stress σ_{mean} is increasing with the silicon layer thickness. In fact, the tip displacement is more sensitive to the platinum layer thickness than the tip temperature because the thermal expansion coefficient of the platinum is three times larger than that of the silicon layer.

In the second group, only the width of the heating circuit and the gap around the middle leg are influential on the objectives. Since the fixed voltage is applied on the heating circuit, a wider heating circuit means a higher heating power and a larger thermal expansion, and consequently a higher tip temperature and a larger tip displacement. A larger gap means softer supporting layer and consequently a larger tip displacement and a lower sensor stress.

In the third group, $T_{\max}$ and $u_{\max}$ are increasing with the widths of the tip gaps and σ_{mean} is not sensitive to the parameters in this group. This is because wide tip gaps implies concentrated heat distribution in the tip and locally soft supporting layer. The tip temperature is also sensitive to the cross section of the heater.

By a preliminary optimization, the original design has been simplified as shown in Figure 3. According to a new sensitivity analysis, the influential parameters namely the width $Wg2$ of the middle gap, the widths Whb and Whu of the heating tracks, the widths Wcb and Wcu of the sensing tracks, the width WJn of the narrow part of the middle leg, the bottom end position $Hfin$ of the heater which also corresponds to the heater length, and the height $Hh2$ of the middle part of the tip gap are selected as active variables.

The results of optimization for $T_{\max}$ and $u_{\max}$ are shown in Figure 4. The coordinates of each plotted point are $(\frac{u_{\max}}{u^0_{\max}}, \frac{T_{\max}}{T^0_{\max}})$ where $u^0_{\max}$ and $T^0_{\max}$ are related to the nominal design. In this approach, all the points along the pareto front correspond to optimal designs but for different compromises. Table 1 reports the chosen design in Figure 4. Compared with the original design, improvements by 300% for $T_{\max}$ (41.6 K vs 10 K) and 90% for $u_{\max}$ (20.67 nm vs 200 nm) were achieved. The piezoresistive sensor stress σ_{mean} is not presented in the two-dimensional graph, however, it has been improved by 3.59%. Those results are significant but simulation time was long, i.e. 12 hours for 1022 samples, each sample requiring a simulation. The average number of FEM elements in each simulation is about 3200 and the average time is 45 s. The simulation

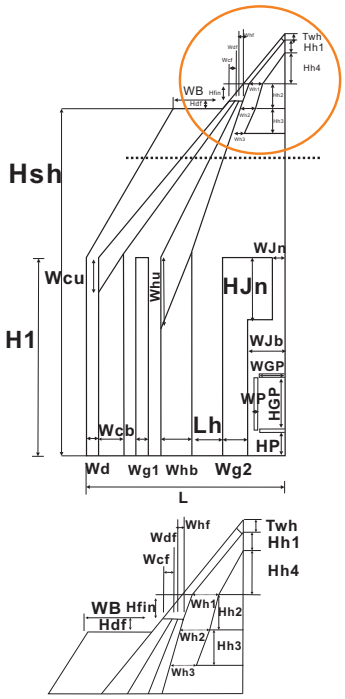

Figure 3. Parametrization of second design

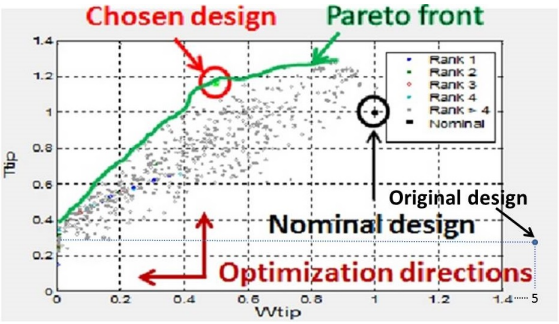

Figure 4. Two-objective optimization

time consists of about 3 s for the setting of COMSOL server environment, 2 s for building the geometry, 3 s for setting equations, 34 s for solving the equations and 3 s for extracting objective features. Considering the relative simplicity of the problem and the low number of active parameters, we consider the total optimization takes far too long so that to be routinely used. Since the number of finite elements cannot be reduced without degrading the accuracy, we have developed a thin plate model, presented in the last section, aimed at simplifying the model and thus to significantly reduce the computation time.

In addition, a robust analysis based on the Monte Carlo method has been applied to the chosen optimal design with 100 samples and a $\pm 10\%$ variation of active variables around the optimal value. Figure 5 shows the result where the optimal design is marked by a black square. The optimal design is considered as robust since it is located close to the center of the 95% confidence ellipse.

Free Variable	Initial	Optimal	Relative value (%)
$Wg2$	22	4.744	21.55
Whb	18	9.979	55.44
Whu	10	9.642	96.42
Wcb	10	1.44	14.4
Wcu	10	2.589	25.89
WJn	5	1.923	38.45
$Hfin$	10	19.74	197.4
$Hh2$	10	3.624	36.24

Table 1. Optimization report

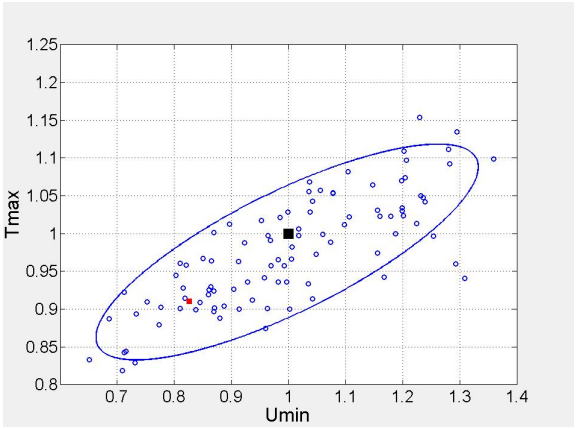

Figure 5. Scatter plot with 95% confidence ellipse

7. Thin plate model

The thin plate model introduced in this section is aimed at reducing the model 1 which is defined on the thin structure Ω. Its derivation is based on an asymptotic method related to the ratio ε between the order of the thickness and that of the width or of the length. Moreover, regarding to the small value of the thermal conductivity $k^{\mathrm{SiO2}} = 1.4$ compared to $k^{\mathrm{Pt}} = 71.6$ and to $k^{\mathrm{Si}} = 34$, we introduce the scaled coefficients

$$k^{\mathrm{Pt},0} = k^{\mathrm{Pt}},\ k^{\mathrm{SiO2},0} = k^{\mathrm{SiO2}}/\varepsilon^2 = 140 \text{ and } k^{\mathrm{Si},0} = k^{\mathrm{Si}},$$

which are almost of the same order. The two-scale transform S used for this model is a linear transformation mapping a function v defined on the three-dimensional domain Ω into Sv a function defined on the product of the two-dimensional mid-plane ω of the plate with an interval J^1 which is a dilation of the thickness by the factor ε. The mid-plane ω is comprise of the projection ω_{Pt} of Ω_{Pt} on the $(x\text{-}y)$-plane and $\omega_S^0 = \omega \backslash \omega_{\mathrm{Pt}}$ the projection of the complementary part. The interval J^1 is also composed of three sub-intervals J^1_{Pt}, J^1_{SiO2} and J^1_{Si}, the scaled thickness of the three layers. We assume that the two-scale transform of each field v involved in the model admits an asymptotic expansion $Sv = \varepsilon^{m_0} v^0 + \varepsilon^{m_0+1} v^1$ where m_0 is determined by a preliminary mathematic analysis. For more detailed information on two-scale analysis, we refer to e.g. [9], but the detailed derivation of the present model differs by some points and will be published in a separate paper.

We introduce the temperature fields $T_{\rm Pt}$, $T_{\rm SiO2}$ and $T_{\rm Si}$ to distinguish between the temperature fields in each layer. The exponent m_0 is equal to -1 in the expansion of $S(u_3)$ and is equal to 0 in the expansion of the other terms.

In the two-scale model of the thermo-electro-mechanical thin probe, the temperatures $T^0_{\rm Pt}$ and $T^0_{\rm Si}$ in the platinium and the silicon layers, the voltage φ^0 and the mechanical displacement u^0_3 are constants in the thickness direction. Moreover, the temperature $T^0_{\rm SiO2}$ of the SiO2 layer is equal to $\lambda(x^1_3-b)+T^0_{\rm Si}$ in $\omega_{\rm Pt}$ with $\lambda = l^{-1}(T^0_{\rm Pt}-T^0_{\rm Si})$, l and b being the length of $J^1_{\rm SiO2}$ and the bottom coordinate of $J^1_{\rm SiO2}$, and $T^0_{\rm SiO2}=T^0_{\rm Si}$ in the other part $\omega\backslash\omega_{\rm Pt}$. Evidently, $T^0_{\rm Pt}$ is defined in $\omega_{\rm Pt}$ only and extended by zero in $\omega\backslash\omega_{\rm Pt}$. The fields $T^0_{\rm Pt}$, $T^0_{\rm Si}$, φ^0 and u^0_3 are solution to the coupled two-dimensional partial differential equations,

$$\left\{\begin{array}{r} -k^{\rm Pt}\Delta T^0_{\rm Pt}+r_{\rm SiO2}k^{\rm SiO2}\lambda = a\Delta\varphi^0 \text{ in } \omega_{\rm Pt}\\ -\operatorname{div}(a\nabla\varphi^0)=0 \text{ in } \omega_{\rm Pt}\\ -k^{\rm Si}\Delta T^0_{\rm Si}-r^{-1}_{\rm Si}r_{\rm SiO2}k^{\rm SiO2}\lambda=0 \text{ in } \omega_{\rm Pt}\\ -k^{\rm Si}\Delta T^0_{\rm Si}=0 \text{ in } \omega\backslash\omega_{\rm Pt}\\ -\partial^2_{\alpha\beta}(m_{\alpha\beta}+T^0_{\rm Pt}M^{\rm Pt}_{\alpha\beta}+T^0_{\rm Si}M^{\rm Si}_{\alpha\beta})=\partial_\alpha q_\alpha+f^H_3 \text{ in } \omega\\ m_{\alpha\beta}=-C^H_{\alpha\beta\theta\gamma}\partial^2_{x^0_\theta x^0_\gamma}u^0_3 \text{ in } \omega. \end{array}\right.$$

The temperature gradient λ in $J^1_{\rm SiO2}$ plays the role of a negative heat source for the equation of $T^0_{\rm Pt}$ and a positive heat source for this of $T^0_{\rm Si}$. Denoting by $\fint_{J^1_{\rm X}} f(x^1_3)\,dx^1_3$ the mean value over $J^1_{\rm X}$, the parameters of the model are the volume ratio $r_{\rm SiO2}$ between $\Omega_{\rm SiO2}$ and Ω, the volume ratio $r_{\rm Si}$ between $\Omega_{\rm Si}$ and Ω, the electric conductivity $a=(1+\alpha T^0_{\rm Pt})^{-1}a^{ref}$, the mean lateral body force $q_\alpha=\fint_{J^1}x^1_3 f_\alpha dx^1_3$ and the mean vertical body force $f^H_3=\fint_{J^1}f_3\,dx^1_3$. The piecewise constant elastic tensor is defined by $C^H_{\alpha\beta\theta\gamma}=\fint_{J^1}(C_{\alpha\beta\theta\gamma}+C_{\alpha\beta k3}(2-\delta_{k3})L^M_{k3\theta\gamma})\left(x^1_3\right)^2dx^1_3$ for $x^0\in\omega_{\rm Pt}$ and by $C^H_{\alpha\beta\theta\gamma}=\fint_{J^1_{\rm SiO2}\cup J^1_{\rm Si}}(C_{\alpha\beta\theta\gamma}+C_{\alpha\beta k3}(2-\delta_{k3})L^M_{k3\theta\gamma})\left(x^1_3\right)^2dx^1_3$ for $x^0\in\omega\backslash\omega_{\rm Pt}$ where the coefficients $L^M_{k3\theta\gamma}$ are solution to $(2-\delta_{k3})C_{i3k3}L^M_{k3\theta\gamma}=C_{i3\theta\gamma}$ for any θ, γ. The three matrices of thermal expansion coefficients are $M^{\rm Pt}_{\alpha\beta}=\frac{|J^1_{\rm Pt}|}{|J^1|}\fint_{J^1_{\rm Pt}}x^1_3M^h_{\alpha\beta}\,dx^1_3+M^{\rm SiO2}$, $M^{\rm Si}_{\alpha\beta}=\frac{|J^1_{\rm Si}|}{|J^1|}\fint_{J^1_{\rm Si}}M^h_{\alpha\beta}x^1_3\,dx^1_3-M^{\rm SiO2}$ for $x^0\in\omega_{\rm Pt}$ and $M^{\rm Si}_{\alpha\beta}=\fint_{J^1_{\rm SiO2}\cup J^1_{\rm Si}}x^1_3M^h_{\alpha\beta}\,dx^1_3$ for $x^0\in\omega\backslash\omega_{\rm Pt}$, where $M^{\rm SiO2}=\frac{|J^1_{\rm SiO2}|}{|J^1|}\fint_{J^1_{\rm SiO2}}l^{-1}(x^1_3-b)M^h_{\alpha\beta}x^1_3\,dx^1_3$ with $M^h_{\alpha\beta}=\delta_{\alpha\beta}M+2C_{\alpha\beta\eta3}L^H_{\eta3}+C_{\alpha\beta33}L^H_{33}$ and the parameters $L^H_{\eta3}$ are solution to $(2-\delta_{k3})C_{i3k3}L^H_{k3}=\delta_{i3}M_{i3}$.

The projection of the boundaries Γ^0, Γ^e_{01} and Γ^e_{02} on the $(x$-$y)$-plane are denoted by γ^0, γ^e_{01} and γ^e_{02}. The temperatures satisfy the boundary conditions $T^0_{\rm Pt}=T^0_{\rm Si}=0$ on γ^0, the voltage source is imposed on γ^e_{01} and γ^e_{02} is grounded. The usual clamping conditions $u_3=\partial_n u_3=0$ apply on γ^0 together with the free load boundary conditions $(m_{\alpha\beta}+T^0_{\rm Si}M^{\rm Si})n_\beta n_\alpha=0$ and $\partial_\tau((m_{\alpha\beta}+T^0_{\rm Si}M^{\rm Si})n_\beta\tau_\alpha)+\partial_\beta(m_{\alpha\beta}+T^0_{\rm Si}M^{\rm Si})n_\alpha=-q_\alpha n_\alpha$ on $\partial\omega\backslash\gamma^0$. Finally, the interfaces between $\omega_{\rm Pt}$ and $\omega\backslash\omega_{\rm Pt}$ are subjected to natural transmission conditions.

This model has not yet been implemented, but we observe that it is posed in a two-dimensional domain instead of a three-dimensional domain which implies a dramatic mesh reduction. Moreover, it involves one more temperature field but two less mechanical displacement fields. In total, we expect a significant simulation time reduction.

8. Conclusion

A novel SThm probe design has been presented with its functioning mode. Various aspects of its modeling, simulation and design have been reported: a tip-surface interaction model, a study of the design optimization, and a two-scale model of the thin probe which should shorten the simulation time.

Acknowledgements

This research effort is sponsored and funded by European FP7 NANOHEAT project and by the Labex ACTION program (contract ANR-11-LABX-01-01).

References

[1] Gerd Binnig, Calvin F Quate, and Ch Gerber. Atomic force microscope. *Physical review letters*, 56(9):930, 1986.

[2] Gerd Binnig and Heinrich Rohrer. Scanning tunneling microscope, August 10 1982. US Patent 4,343,993.

[3] RB Dinwiddie, RJ Pylkki, and PE West. Thermal conductivity contrast imaging with a scanning thermal microscope. *Thermal conductivity*, 22:668–668, 1993.

[4] B. Gotsmann and M. A. Lantz. Quantized thermal transport across contacts of rough surfaces. *Nat Mater*, 12(1):59–65, January 2013.

[5] B Gotsmann, MA Lanz, A Knoll, and U Dürig. Nanoscale thermal and mechanical interaction studies using heatable probes. *Nanotechnology, Volume 6: Nanoprobes*, Jan 2009.

[6] Wen-Pin Hsieh, Bin Chen, Jie Li, Pawel Keblinski, and David G Cahill. Pressure tuning of the thermal conductivity of the layered muscovite crystal. *Physical Review B*, 80(18):180302, 2009.

[7] P Janus, D Szmigiel, M Weisheit, G Wielgoszewski, Y Ritz, P Grabiec, M Hecker, T Gotszalk, P Sulecki, and E Zschech. Novel sthm nanoprobe for thermal properties investigation of micro-and nanoelectronic devices. *Microelectronic Engineering*, 87(5):1370–1374, 2010.

[8] G Jóźwiak, D Kopiec, P Zawieruch, T Gotszalk, P Janus, P Grabiec, and IW Rangelow. The spring constant calibration of the piezoresistive cantilever based biosensor. *Procedia Engineering*, 5:838–841, 2010.

[9] M. Lenczner and R. C. Smith. A two-scale model for an array of AFM's cantilever in the static case. *Mathematical and Computer Modelling*, 46(5-6):776–805, 2007.

[10] Yifei Mo, Kevin T. Turner, and Izabela Szlufarska. Friction laws at the nanoscale. *Nature*, 457(7233):1116–1119, February 2009.

[11] B N J Persson, A I Volokitin, and H Ueba. Phononic heat transfer across an interface: thermal boundary resistance. *Journal of Physics: Condensed Matter*, 23(4):045009, 2011.

[12] R. Prasher. Acoustic mismatch model for thermal contact resistance of van der Waals contacts. *Applied Physics Letters*, 94(4):041905, 2009.

[13] RS Prasher and PE Phelan. Microscopic and macroscopic thermal contact resistances of pressed mechanical contacts. *Journal of Applied Physics*, 100:063538, 2006.

[14] Li Shi and Arunava Majumdar. Thermal transport mechanisms at nanoscale point contacts. *Journal of Heat Transfer*, 124(2):329–337, July 2001.

[15] E. T. Swartz and R. O. Pohl. Thermal boundary resistance. *Rev. Mod. Phys.*, 61:605–668, Jul 1989.

[16] RF Szeloch, Teodor P Gotszalk, and P Janus. Scanning thermal microscopy in microsystem reliability analysis. *Microelectronics Reliability*, 42(9-11):1719–1722, 2002.